Combination of Eulerian and ray-tracing approaches for copper laser welding simulation

Julien Daligault, Morgan Dal, Cyril Gorny, Frédéric Coste, Rémy Fabbro

Journal of Laser Applications

Combination of Eulerian and ray-tracing approaches for copper laser welding simulation

Cite as: J. Laser Appl. **34**, 042042 (2022); https://doi.org/10.2351/7.0000786
Submitted: 27 June 2022 • Accepted: 07 October 2022 • Published Online: 04 November 2022

Julien Daligault, Morgan Dal, Cyril Gorny, et al.

Journal of Laser Applications ARTICLE scitation.org/journal/jla

Combination of Eulerian and ray-tracing approaches for copper laser welding simulation

Cite as: J. Laser Appl. 34, 042042 (2022); doi: 10.2351/7.0000786
Submitted: 27 June 2022 · Accepted: 7 October 2022 ·
Published Online: 4 November 2022

Julien Daligault,[a] Morgan Dal, Cyril Gorny, Frédéric Coste, and Rémy Fabbro

AFFILIATIONS

PIMM Laboratory, Arts et Métiers Institute of Technology (Paris), CNRS, CNAM, HESAM University, 151 Boulevard de l'Hôpital, 75013 Paris, France

Note: Paper published as part of the special topic on Proceedings of the International Congress of Applications of Lasers & Electro-Optics 2022.

[a]**Author to whom correspondence should be addressed; electronic mail:** julien.daligault@ensam.eu

ABSTRACT

Laser welding of pure copper and its alloys is a challenging process with a growing industrial interest due to the latest development in the field of electric mobility. The difficulties are mainly related to the material's high thermal conductivity and a poor absorptivity of few percent at the classical IR laser (YAG). It is also well known that such a configuration can lead to the formation of undesirable defects, such as pores or spatters as a consequence of melt pool instabilities. It has been observed experimentally that the usage of a laser at both high speed and high power tends to limit those instabilities. Although this positive influence has already been observed for equivalent materials, a physical explanation is not yet available. In this perspective, a multiphysical simulation of the process at the melt pool scale is currently being developed by using COMSOL MULTIPHYSICS® software. The latter includes an Eulerian interface tracking method for the liquid-gas interface (phase field) and a ray-tracing description of the laser beam to take into account the well-known beam trapping effect under a keyhole regime. For the sake of time computation, the numerical model is first developed in an axisymmetric coordinate system (r,z) to be representative of a laser spot welding process and to validate the numerical coupling methodology. The model will then be extended to a 3D welding case and used as a predictive tool to make appropriate choices on welding parameters to obtain good quality welds (stable melt pool, low porosity rate, etc.).

Key words: laser welding, copper, finite elements, interface tracking, ray-tracing

I. INTRODUCTION

Copper's electrical and thermal properties make it an ideal material candidate for numerous applications in an electrical mobility domain. On the other hand, with a judicious choice of process parameters, using an assembly process such as laser welding allows for the most metallic material to produce a regular deep weld seam repeatedly and at a high production rate.[1–3]

During the laser beam process, a high-energy laser beam interacts with free electrons at the surface of one or several samples (Fig. 1) whose temperature rises until a molten pool is formed. If the energy absorbed by the material is high enough, the irradiated surface reaches its boiling temperature and a vaporization process is initiated. By an action-reaction principle, the evaporated matter induces a recoil pressure at the surrounding-gas/liquid-metal interface that tends to deform the molten pool and push the liquid out of the interaction zone. The vapor capillary created by this process is usually referred to as a "keyhole" inside which the laser undergoes specular reflections. This phenomenon creates important local irradiance variations[2–4] and increases the laser-matter coupling as confirmed by absorptance measurements through integrating spheres[5–9] or a calorimeter.[10] This phenomenon is well known in laser welding and is referred to as a "multiple reflections effect" or "beam trapping effect." Those high irradiance peaks locally heat the matter and create variable vaporization intensities along the capillary resulting in hydrodynamic instabilities in the molten pool.

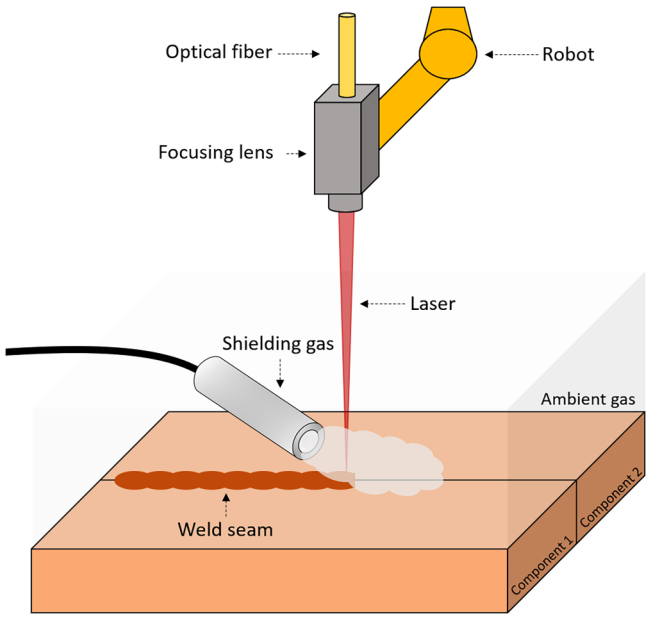

FIG. 1. Welding setup illustration.

On the other hand, the induced vapor jet also greatly influences the molten pool dynamics as vapor brings momentum to the impacted liquid. This is typically the case when process parameters lead to a single wave welding regime[11] where the keyhole front is inclined and the vapor plume is oriented at the rear molten pool. In this configuration, vapor can cause fluctuations at the liquid-gas interface or even melt droplets ejected out of the interaction zone.

For most materials, those instabilities can be avoided with a relevant choice of process parameters. However, the assembly of both highly reflective and thermally conductive materials such as aluminum or copper through laser welding is still a noteworthy challenge. For example, Mattern[12] presents the influence of copper property variations such as absorptivity (due to surface oxidation, roughness, etc.) on the intensity needed to melt and vaporize the sample, showing a lack of repeatability of the process, with a simplified thermal simulation for copper conduction laser welding. Heider[13] observed by means of x-ray imaging the generation process of spatters in copper laser welding and showed that the formation of bubbles inside the capillary leads to spatters and pores during the process. To overcome those process instabilities, Heider *et al.*[14] used high laser power (until 16 kW). At 10 kW and above (with a 200 μm laser spot diameter), they were able to reach a penetration depth of several millimeters (up to 6.5 mm) without any weld defects. Other authors used a green laser, which is more absorbed by copper (approx. 40%) than IR laser (approx. 5%)[7,12,15] at room temperature. Alter *et al.*[16] used a green laser up to 4 kW and were able to obtain high quality welds free of spatters at high welding speed at least for conduction mode. Hess *et al.*[17] combined an IR laser with a green laser and showed that a low-power green laser could significantly improve the welding quality of copper alloys and reduce IR power needed to initiate keyhole mode. Another method to enhance copper weld quality is by modulating laser power. With this approach, laser beam power is modulated at a certain frequency around a mean power. Heider *et al.*[18,19] showed that power modulation on copper laser welding significantly reduces weld defects quantity while increasing penetration depth compared to cases at the same constant laser power.

Even though the recent emergence of x-ray *in situ* measurements allows the observation of keyhole dynamics and defect formation mechanisms,[8,13,19,20] information such as irradiance or vapor plume hydrodynamic inside the capillary cannot be obtained directly from these experiments. In this context, numerous numerical tools have been developed over the past years aiming to give a complete picture of the process at the melt pool scale. For these experiments, the key parameter seems to be the heat input coming from the laser beam.[3,4] One of the "simplest" ways to take into account the beam trapping effect is through an equivalent heat source coupled with an artificially increased absorptance inside the capillary.[21] While giving relatively satisfactory keyhole penetration dynamics, this method does not give an accurate laser deposition along the keyhole wall and, thus, potential resulting instabilities. A more physical approach to modeling the laser beam is through Maxwell's equations computation. Courtois *et al.*[5] developed a self-consistent model using this electromagnetic approach in combination with an Eulerian interface tracking method (level-set) for a laser spot welding simulation and found good agreement with experimental results. However, to the best of our knowledge, this model has never been implemented in a complete 3D laser welding description due to the need for high computation resources. An intermediate solution chosen by many authors is the ray-tracing description of the laser beam where a finite amount of rays interact with the keyhole wall and gives an energy deposition including multiple reflections effect. As Ki *et al.*[22] and Medale *et al.*[6] presented in early works, a self-consistent model of both laser drilling and welding and focused on the laser irradiance distribution along the keyhole wall. Mayi *et al.*[4] recently compared a complete multiphysical simulation including a ray-tracing description with up-to-date experimental x-ray measurements.[8] Transient keyholes formation mechanisms were, thus, highlighted and supported by experiments. More recently, Liu *et al.*[23,24] developed a self-consistent welding model, including Crooker *et al.*'s[25] Gaussian beam representation by rays allowing them to take into account the laser beam defocusing effect.

In this contribution, a numerical model is being developed under COMSOL MULTIPHYSICS® including a ray-tracing description of the laser beam coupled with a phase-field approach for the interface tracking problem. The model is currently developed in a 2D-axisymmetrical coordinate system (r,z) to deal with the already high computation costs due to the involved physics. The model also includes thermal dependency of most material properties, recoil pressure, and surface tension effects. Results are then compared to laser spot welding experimental results on Cu-ETP material.

II. COMPUTATIONAL MODEL

A. Interface tracking: Phase field

The Cahn–Hilliard equation is computed in order to get the transport of a variable ϕ representing a smoothed transition

between two distinct materials (copper and ambient gas in this case) in a single computational domain. This fourth-order partial differential equation is instead solved as two coupled second-order equations using an additional variable ψ,[26]

$$\frac{\partial \phi}{\partial t} + \vec{u} \cdot \vec{\nabla}\phi = \vec{\nabla} \cdot \left(\frac{3}{2\sqrt{2}} \sigma \epsilon \chi \vec{\nabla} \psi \right), \tag{1}$$

$$\psi = -\vec{\nabla} \cdot (\epsilon^2 \vec{\nabla}\phi) + (\phi^2 - 1)\phi, \tag{2}$$

where $\vec{u}$ is the velocity field ($m\,s^{-1}$) computed with mass (6) and momentum (7) conservation equations, σ is the surface tension coefficient ($N\,m^{-1}$) between liquid metal and ambient gas, ϵ is a parameter controlling interface thickness (m), and χ is a mobility tuning parameter ($m\,s\,kg^{-1}$).

The phase field can be initialized analytically with a hyperbolic tangent,

$$\phi_0 = -\tanh\left(\frac{z - z_0}{\sqrt{2}\epsilon} \right). \tag{3}$$

Equation (3) gives a distribution where $\phi = -1$ under z_0, $\phi = 1$ above z_0 and a smooth transition at z_0.

The phase field variable ϕ is then used to differentiate local physical properties X (ρ, μ, λ, etc.) used in energy, mass, and momentum conservation equations,

$$X = \left(\frac{1 - \phi}{2} \right) X_{gas} + \left(\frac{1 + \phi}{2} \right) X_{metal}. \tag{4}$$

Finally, the δ-function used to introduce boundary conditions at the material transition is approximated by a smoothed function according to

$$\delta = 6|\vec{\nabla}\phi||\phi(1 - \phi)|. \tag{5}$$

B. Fluid dynamics: Navier–Stokes

Mass (6) and momentum (7) conservation equations are solved in their incompressible form to compute velocity and pressure fields,

$$\vec{\nabla} \cdot \vec{u} = 0, \tag{6}$$

$$\rho \frac{\partial \vec{u}}{\partial t} + \rho(\vec{u}.\vec{\nabla})\vec{u} = \vec{\nabla} \cdot \left(-pI + \mu[\vec{\nabla}\vec{u} + (\vec{\nabla}\vec{u})^T] \right) + \overrightarrow{F_v}, \tag{7}$$

where ρ and μ are, respectively, local density and dynamic viscosity obtained with (4) and $\overrightarrow{F_v}$ are the volume forces. Recoil pressure (8), surface tension (9), and Marangoni effect (10) are introduced through volume forces in momentum balance,

$$\overrightarrow{F_{rec}} = p_{rec}(T)\delta\vec{n}, \tag{8}$$

$$\overrightarrow{F_s} = \sigma\kappa\delta\vec{n}, \tag{9}$$

$$\overrightarrow{F_m} = \frac{\partial \sigma}{\partial T} \overrightarrow{\nabla_s} T, \tag{10}$$

where κ is the interface curvature and $\overrightarrow{\nabla_s} = (I - nn^T)\vec{\nabla}$ is the surface gradient. Recoil pressure p_{rec} is expressed as a function of the saturated vapor pressure p_{sat} and β_r the retrodiffusion coefficient,

$$p_{sat}(T) = p_0 \exp\left[\frac{ML_v}{RT_v} \left(1 - \frac{T_v}{T} \right) \right], \tag{11}$$

$$p_{rec}(T) = \frac{1 + \beta_r}{2} p_{sat}(T). \tag{12}$$

In Eq. (11), p_0 corresponds to the ambient pressure (Pa), M the molar mass ($kg\,mol^{-1}$), L_v to the enthalpy of vaporization ($J\,kg^{-1}$), R to the gas constant ($J\,mol^{-1}\,K^{-1}$), T_v and T, respectively, to the vaporization and local temperatures (K). In this case, vapor plume effect is only modeled through a pressure effect at the interface but no plume is generated.

Finally the solid-liquid metal behavior is introduced through an enhanced dynamic viscosity defined as follows:[21]

$$\mu = \begin{cases} 1000\ \text{Pa s} & \text{for } T < T_m, \\ \mu_{metal}(T) & \text{for } T \geq T_m. \end{cases} \tag{13}$$

C. Heat transfers

Heat conservation equation is solved to compute the temperature field in the computational domain,

$$\rho c_p^{eq} \frac{\partial T}{\partial t} + \rho c_p^{eq}(\vec{u}.\vec{\nabla}T) - \vec{\nabla} \cdot (\lambda \vec{\nabla} T) = Q_{abs} - Q_{loss}, \tag{14}$$

where c_p and λ are, respectively, the local specific heat ($J\,kg^{-1}\,K^{-1}$) and thermal conductivity ($W\,m^{-1}\,K^{-1}$).

The solid-liquid metal phase change is expressed through an equivalent heat capacity including the latent heat of fusion L_m,[4,5,21]

$$c_p^{eq} = c_p + \frac{L_m}{\sqrt{\pi}\Delta T_m} \exp\left(-\frac{(T - T_m)^2}{\Delta T_m^2} \right). \tag{15}$$

T_m represents the melting point (K) and ΔT_m the solidification range (K). Even though pure copper is modeled (i.e., no physical solidification interval), a numerical parameter range is taken as 50 K, which is introduced to improve computational stability.

The absorbed volume heat source Q_{abs} is the absorbed irradiance q_{abs} (times the δ-function) obtained through ray-tracing method detailed in Sec. II D. The volume heat losses Q_{loss} includes radiation, evaporation, and convection losses defined as

$$Q_{loss} = [\epsilon\sigma_{sb}(T^4 - T_0^4) + \dot{m}(T)L_v + h(T - T_0)]\delta. \tag{16}$$

In Eq. (16), ϵ corresponds to the metal emissivity, σ_{sb} the Stefan–Boltzmann constant ($kg\,s^{-3}\,K^{-4}$), T_0 the room temperature (K), and h the convection coefficient ($W\,m^{-2}\,K^{-1}$).

The ablation rate $\dot{m}$ is expressed as

$$\dot{m} = (1 - \beta_r)\sqrt{\frac{M}{2\pi RT}} p_{sat}(T). \quad (17)$$

D. Ray-tracing-Eulerian coupling

Ray-tracing computation is coupled with the phase-field Eulerian interface tracking method through a dedicated algorithm developed with COMSOL MULTIPHYSICS® JAVA programming mode.

A first component is used to solve energy (14), mass (6), and momentum conservation (7) equations. Once a stop criterion is reached based on the absolute difference between current and initial values of the normalized δ-function (18), the multiphysical study is stopped. This criterion allows the update of the irradiance distribution once a critical geometrical deformation occurs. Smaller values of C_{max} means more frequent updates and conversely,

$$\max\left(\left|\left(\frac{\delta}{\delta_{max}}\right)_t - \left(\frac{\delta}{\delta_{max}}\right)_{t_0}\right|\right) \geq C_{max}. \quad (18)$$

Iso-value of $\phi = 0$ is then extracted and used to reconstruct a physical boundary in a second component where ray-tracing is computed. Eikonal equation is solved for a set of N_r rays—each carrying a fraction of the laser power (19)—and are distributed homogeneously along r-axis until laser radius is reached, modeling a top-hat distribution,

$$P_{rays,init} = \frac{P}{N_r}. \quad (19)$$

Each ray is subjected to multiple specular reflections within the reconstructed capillary and transfers a fraction of its power equals to the material absorptivity α. Absorbed power is accumulated locally along the capillary. Once divided by local mesh size, the absorbed irradiance q_{abs}, thus, obtained is reinjected in the energy conservation equation,

$$P_{acc} = \sum_{i=1}^{N_r} \sum_{j=1}^{N_{refl}} \alpha P_{i,j} \vec{k}_{i,j} \cdot \vec{n}. \quad (20)$$

An illustration of the coupling method is presented in Fig. 2.

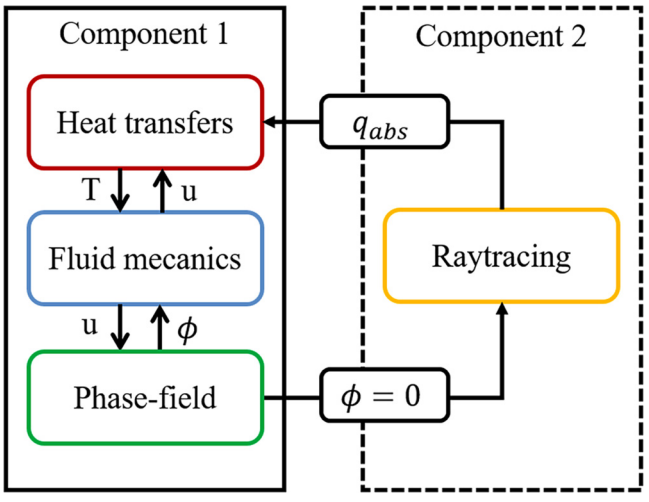

FIG. 2. Ray-tracing and multiphysics components coupling.

E. Geometrical assumptions

2D-axisymmetrical (r,z) representation is used for static laser shots modeling. Corresponding computational domain and mesh are represented in Fig. 3. A fine grid mesh is used around r- and z-axis where liquid-gas interface is expected to be computed during the simulation. Note that mesh represented in Fig. 3 is coarse on purpose to highlight the different regions. The actual mesh size in the refined zone is approximately 8 μm leading to around 400 000 degrees of freedom.

F. Material properties

Copper physical properties are implemented using temperature dependent evolution presented in Ref. 27. Ambient gas physical properties are compiled from Ref. 28.

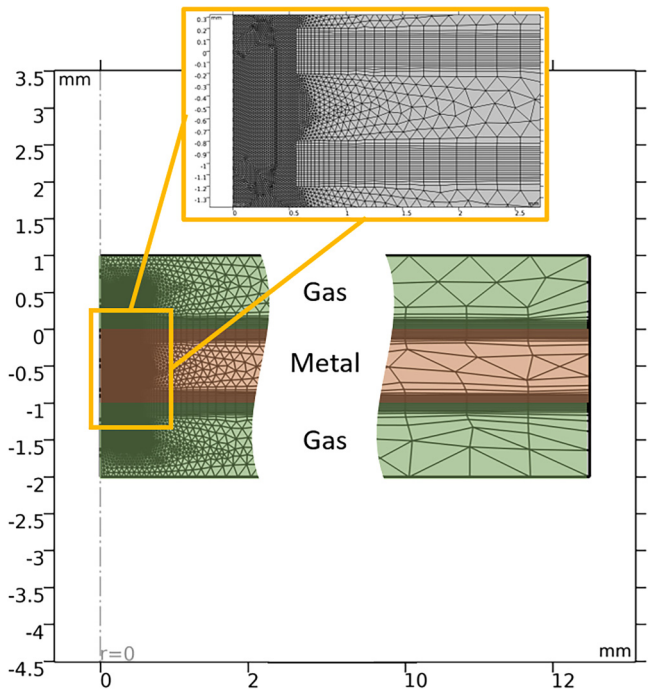

FIG. 3. Computation domain and mesh used for 2D-axisymmetrical laser spot welding simulations.

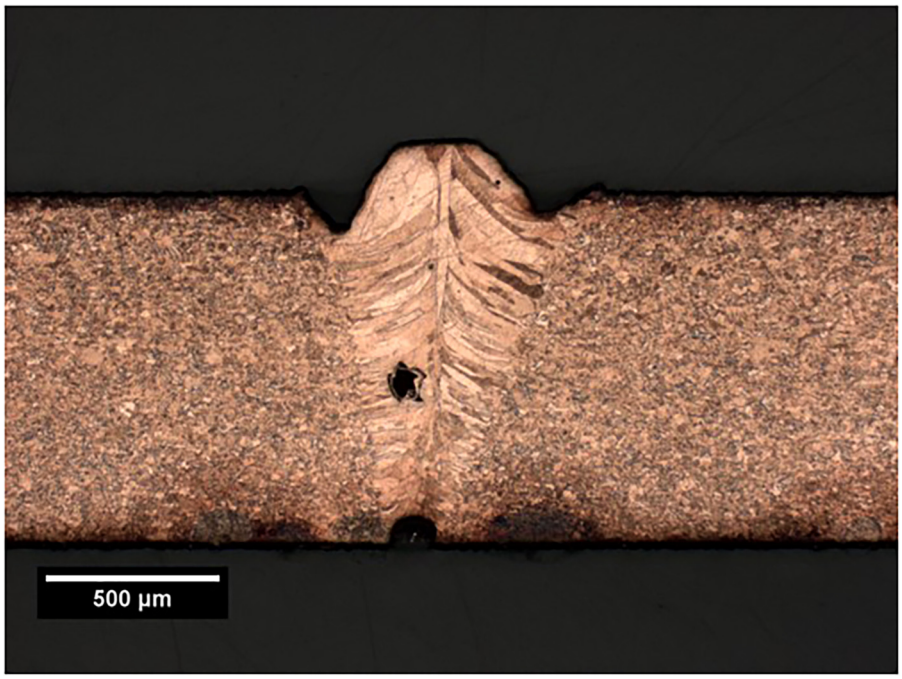

FIG. 4. Microstructure observation in the laser shot symmetry plane. $P = 7$ kW, $d = 560\,\mu$m after 7.5 ms pulse duration.

III. EXPERIMENTAL VALIDATION

To validate the numerical model, a series of experimental laser spot welding is performed at different laser powers and pulse durations to compare the depth and shape of the melt pool over time.

A TruDisk 10002 disk laser with a 1.03 μm wavelength is used for the experiments. The measured beam diameter is 560 μm and remains constant for the whole set of experiments. Laser shots were performed on Cu-ETP disks of 1 mm thickness and 2.5 cm diameter. Samples were placed in a chamber filled in argon with an oxygen analyzer (<100 ppm for each experiment) to avoid oxidation during the process and ease comparison to numerical results. Samples were tilted by 5° to prevent optics from back reflection damages. No specific treatments were applied on samples surface meaning roughness and oxidation might modify the local absorptivity of the material. This topic is discussed in Sec. IV.

Experiments under laser power of 7 and 8 kW were conducted using various pulse durations "t_{pulse}" in order to capture the evolution of depth and shape of the melt pool as a function of time. A first set of static laser shots is performed to find the minimum interaction time required to penetrate the whole sample. For 7 kW static laser shots, an interaction time of 7.5 ms lead to a full melt pool penetration whereas 4 ms were sufficient for 8 kW shots.

Samples are then cross-section cut and mirror polished (with 1 μm diamond solution) in the laser symmetry plan. The microstructure is revealed using a solution composed of 5 ml picric acid (12 g/l), 15 ml acetic acid (99%–100%), 10 ml chlorhydric acid (37%), and 30 ml ethanol. The typical microstructure is presented in Fig. 4. A porosity formed in the resolidified metal and undercuts at the sides of the weld seam are observed.

The laser electrical signal is obtained through an oscilloscope measurement and is presented in Fig. 5. This profile is then fitted for numerical simulation. A rising time constant τ_1 of 40 μs is measured while a decreasing time constant τ_2 of 80 μs is used to fit experimental data.

IV. RESULTS AND DISCUSSION

A. Laser spot welding simulations

Laser spot welding using a top-hat distribution with a beam diameter of 560 μm at 7 kW ($I = 2.8$ MW cm^{-2}) and 8 kW ($I = 3.2$ MW cm^{-2}) are simulated using the model described in Sec. II.

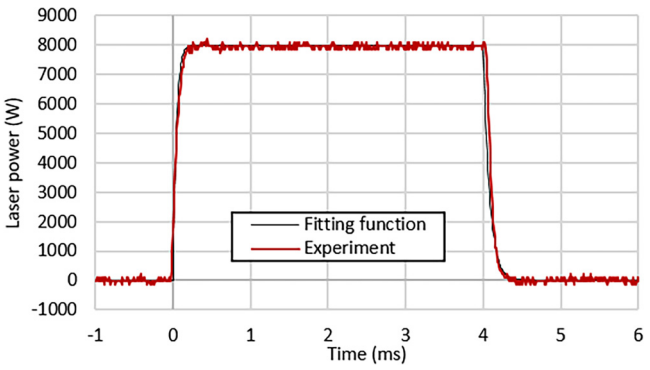

FIG. 5. Laser profile (black curve) fitted for simulation laser power evolution (red dots) measured during a 8 kW shot of 4 ms.

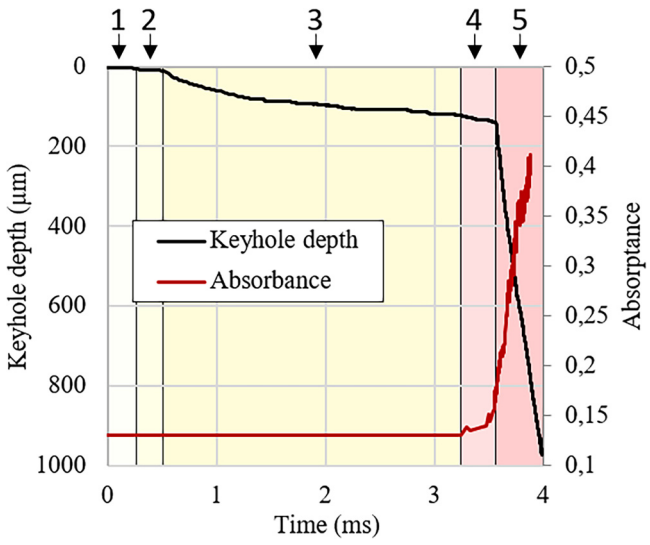

FIG. 6. Keyhole depth (black curve) and total absorptance (red curve) evolution during a 4 ms static laser shot of $P = 8$ kW, $d = 560\,\mu$m.

In both simulations, melt pool and keyhole formation is composed of five steps as already described by Mayi *et al.*[4] Obtained results with a 8 kW laser power are described (Fig. 6): (1) laser power is increasing according to Fig. 5 and sample's surface is rising in temperature. The molten pool is not yet formed and absorptance measured is equal to material absorptivity (from 0 to 0.3 ms), (2) sample reaches the fusion point and the melt pool starts to form under a laser. Thermocapillary convection caused by Marangoni shear stress occurs inside the molten pool and liquid metal circulates from the center of the laser-matter interaction to its side (thermocapillary coefficient $\partial\sigma/\partial T$ being negative). In this step, the molten pool depth reaches tens of micrometers. Hence, no multiple reflections occur yet and the absorptance is still equal to material absorptivity (from 0.3 to 0.6 ms). (3) Afterward, the surface temperature exceeds boiling point and a vaporization process takes place. The induced recoil pressure applied at the liquid-gas interface pushes liquid metal out of the interaction zone and a vapor capillary of nearly 100 μm depth is created. No variation in the absorptance is observed, meaning the liquid-gas geometry leads to an incident top-hat distribution without multiple reflections (from 0.6 to 3.2 ms).

In the next step (4), the vaporization described above still leads to a deeper penetration of the molten pool until 135 μm. Molten pool now reaches the penetration depth above 100 μm and first multiple reflections occur in this induced optical cavity. Absorptance fluctuations of few percent are observed. Rays are observed to be reflected at the sides of the capillary leading to a modified absorbed irradiance along the interface. Locally focused rays induce an increase in temperature that in return deforms the molten pool under the recoil pressure effect. The vapor capillary oscillates between V- and U-shapes as described in Refs. 4 and 8 while the molten pool keeps penetrating into the sample. No major modification in the depth penetration dynamic is observed at this step (from 3.2 to 3.5 ms) as ray reflections are distributed quite homogeneously along the keyhole wall. Finally, (5) at 3.5 ms, the capillary reaches a critical aspect ratio where an important amount of rays and reflections are located at the center of the interaction zone leading to a local absorbed irradiance 60–80 times higher than incident irradiance (without multiple reflections). Depth penetration dynamic is, thus, rapidly increased as observed in Fig. 6 and the molten pool reaches sample thickness within the next 0.5 ms. Figure 7 illustrates the keyhole formation process.

It is also interesting to analyze the evolution of absorptance inside the capillary as a function of the aspect ratio obtained with this self-consistent simulation and compare it with analytical laws often used in simplified models. In Fig. 8, Gouffé's[29] analytical

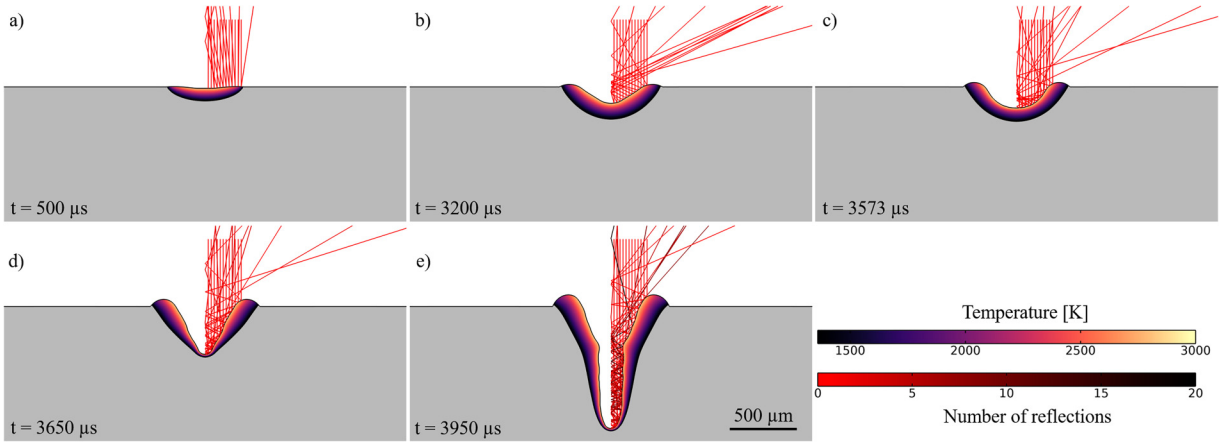

FIG. 7. Keyhole process formation. (a) Pure conduction mode, (b) melt pool deformed through the recoil pressure effect, (c) multiple reflections occur in the capillary, (d) rays focus at the tip of the keyhole rapidly increasing penetration dynamic, and (e) deep keyhole mode. Process parameters are $P = 8$ kW, $d = 560\,\mu$m for a pulse duration $t_{pulse} = 4$ ms.

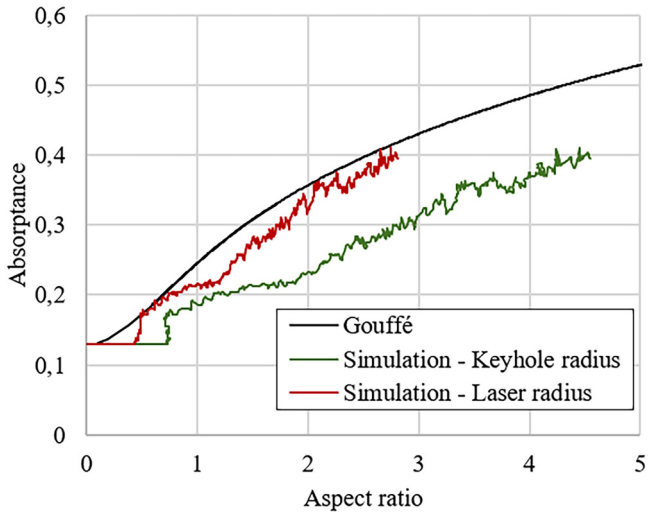

FIG. 8. Evolution of the absorptance inside the capillary with respect to its aspect ratio. Gouffé's (Ref. 29) analytical evolution (black curve) compared to numerical results (green and red curves).

evolution of the absorptance (applied for copper with a 13% incident absorptivity) inside a predefined geometry is presented—here a cone shape—as a function of its aspect ratio defined as the depth of the capillary over its aperture radius. Numerical results obtained with P = 8 kW and d = 560 μm for a pulse duration are also plotted with two considerations. Red curve represents the evolution of absorptance as a function of the keyhole depth over laser beam radius whereas the green curve represents it as a function of the keyhole depth over keyhole aperture radius measured at the sample's surface (z = 0). It can be seen that numerical results present a mode transition from material incident absorptivity—here 13%—to multiple reflections modified absorptance at an aspect ratio of, respectively, 0.5 and 0.75. The difference between the two transitions is easily explained by the fact that the laser beam radius is bigger than the keyhole aperture radius as Fig. 7 illustrates. Hence, the aspect ratio computed with the laser beam radius squeezes the values to lower aspect ratios. After the transition, red and green curves globally follow the same trend as Gouffé's predicts. However, some discrepancies are found as the keyhole shape is not a perfect cone shape assumed by Gouffé.

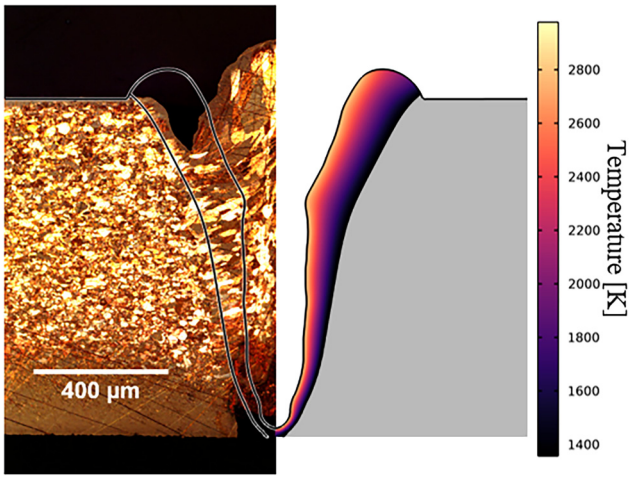

FIG. 9. Weld seam comparison between experimental (left) and simulation (right); computed temperature field (K) is also plotted. Numerical fusion front is reported on experimental cross section as black lines.

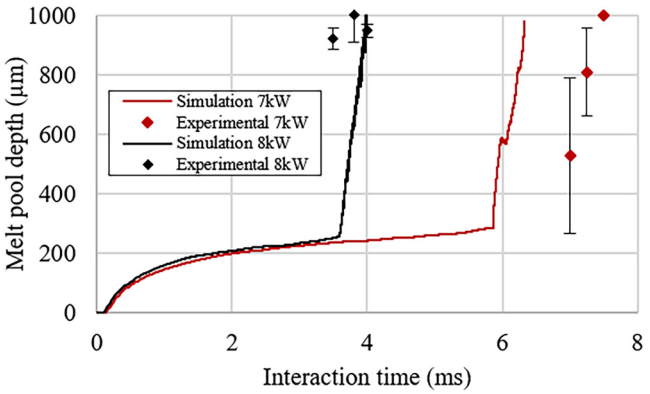

FIG. 10. Simulation results (7 kW red curve, 8 kW black curve) compared to experimental results (7 kW red dots, 8 kW black dots).

B. Results comparison

Experimentally and numerically obtained melt pool shapes are compared. An example of such a comparison is presented on Fig. 9

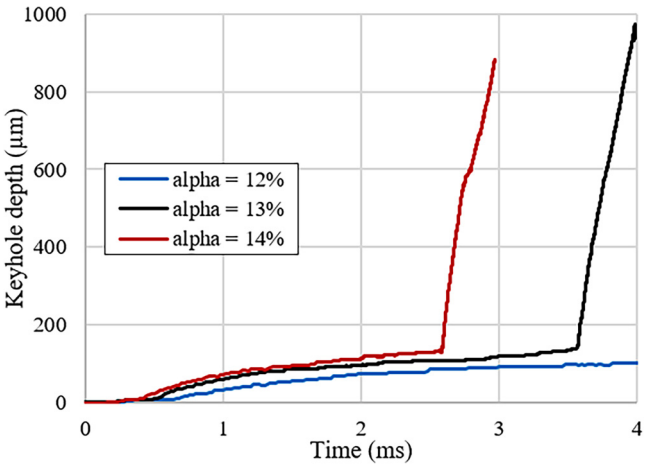

FIG. 11. Sensitivity analysis of absorptivity variations on keyhole penetration dynamic.

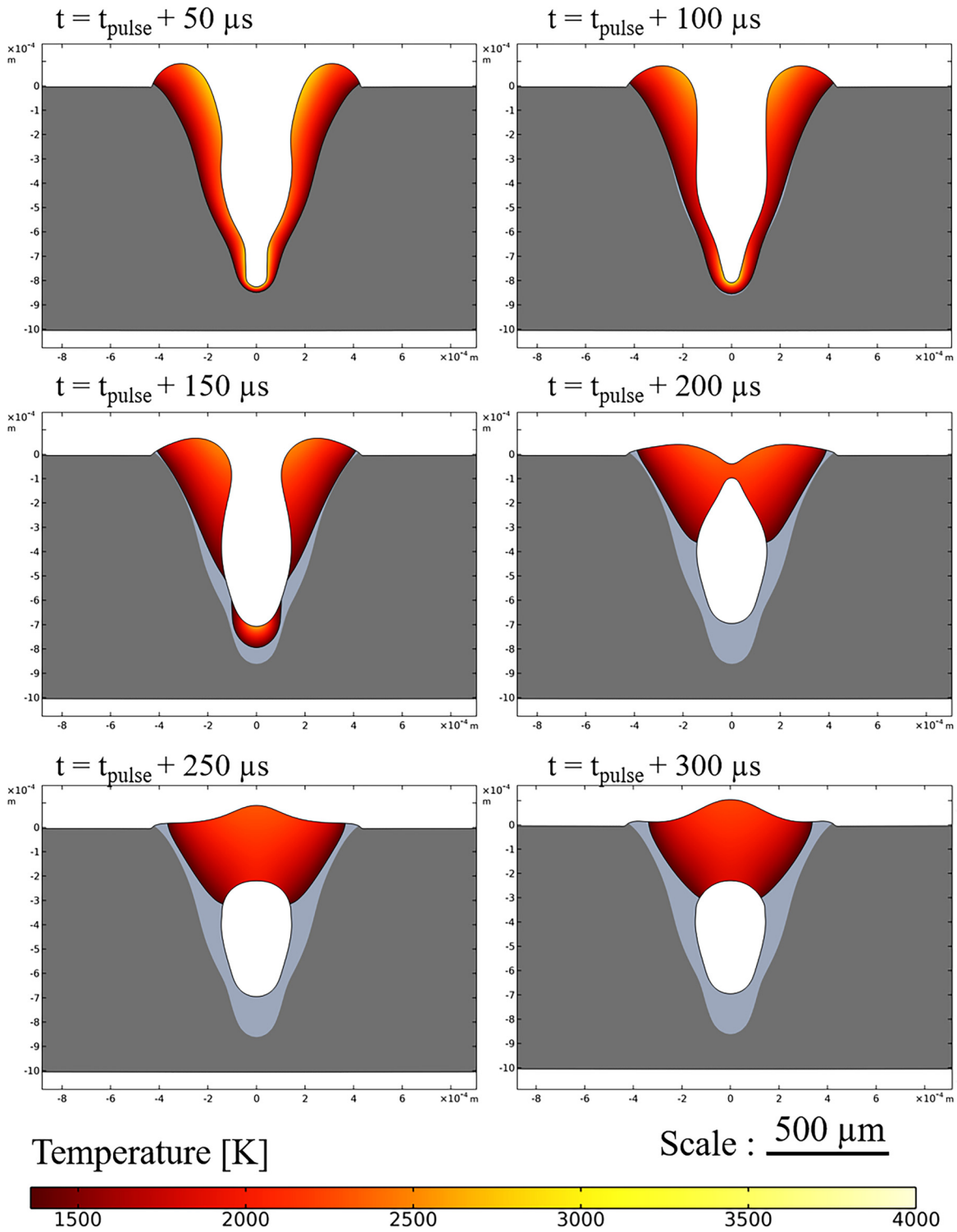

FIG. 12. Porosity formation process during the cooling phase.

for a 8 kW laser shot during 3.8 ms. An experimental melt pool is measured where the grain structure has been modified after melt pool resolidification. A good agreement is found between the simulated melt pool and the experimentally measured one.

Numerical melt pool depth penetration results are compared to experimental measurements in Fig. 10. For 7 kW laser shots, experimental results also present a sharp transition between forced conduction and deep penetration keyhole mode[4,8] with a fast keyhole depth evolution of around 7 ms. However, a time delay of about 1 ms between transitions found numerically and experimentally is observed. This time delay can be explained by a poor knowledge on copper absorptivity or more generally material absorptivity evolution with temperature or other parameters (oxidation, roughness, etc.). Here, the absorptivity is taken constant and equal to 13% compared to 5% in solid and 10% in the liquid state found experimentally by Engler *et al.*[15] This kind of absorptivity modification has already been implemented by other authors.[4,30] A sensitivity analysis of material absorptivity on keyhole penetration dynamic is performed to illustrate this point and is presented in Sec. IV C. Experimental measurements at 8 kW do not capture the previously presented sharp transition but still confirm the range of pulse duration (around 4 ms) needed for a fully penetrated sample of 1 mm. Large error bars presented in Fig. 10 are due to: (1) a small amount of samples observed experimentally, (2) a difficulty with this experiment to find the exact center of the laser shots leading to an uncertainty in the measure, and (3) a poor repeatability of the process already explained by variations of the local absorptivity with oxidation or roughness, which leads to different penetration dynamics between distinct samples. However, this experimental setup does not require heavy installations, such as x-ray measurements, and allows a first depth analysis in laser spot welding. For further study and model-to-experiment comparison, x-ray measurements[19] could be used for a more accurate keyhole penetration depth and shape analysis.

C. Absorptivity analysis

Local material absorptivity is influenced by laser wavelength,[31] surface roughness,[32] oxidation, or local temperature.[15] Engler *et al.*,[15] for example, measured through an integrating sphere the absorption at different material states. For solid state copper alloys, an absorptivity of 4%–8% has been found compared to 8%–10% in the conduction regime giving an idea of the absorptivity in the liquid state. The oxidation effect is also measured and is found to greatly influence the absorption. Compared to the 4%–8% found for a solid phase on a standard sample, those subjected to 30 min at 200 °C led to an increase in absorption between 26% and 34%, i.e., a ratio of 5 on average. Note that an absorptivity of 13% was used in the simulation compared to the 8%–10% proposed by Engler.

The effect of such material absorptivity variation on the melt pool penetration dynamic is observed with a sensitivity analysis on three different case parameters. Material absorptivity is numerically modified at 12%, 13%, and 14% to simulate the effect of material properties variations due to oxidation, roughness, and the lack of knowledge on real temperature dependency. Results are presented in Fig. 11 for spot laser welding simulation at $P = 8$ kW and $d = 560\,\mu$m. The blue curve (12%) leads to a penetration depth of $100\,\mu$m after 4 ms pulse duration insufficient to initiate multiple reflections effect. The black curve (13%) is already described in the laser spot welding simulations section. Finally, the red curve (14%) presents the same penetration dynamics as the black curve (13%) but shifted in time by approximately 1 ms. This simple study shows that a small variation in absorptivity can greatly influence penetration dynamic regarding time evolution.

In fact, a constant material absorptivity property as it is used in the simulation is not representative of the real physics. For a proper representation, each effect should be taken into account separately. For example, a surface roughness or oxidation can hardly be defined for the liquid state. In next development steps, all these effects should be considered separately with their regarding influence on absorptivity.

D. Porosity formation

After the pulse duration is reached, laser power slowly decreased according to Fig. 5. The temperature inside the molten pool decreased accordingly and recoil pressure is no longer the main force driving melt pool dynamics. Surface tension effects tend to close the keyhole as presented in Fig. 12. Hundreds of microseconds after the beginning of the cooling phase a gas bubble is being trapped inside the molten pool. In the present example, the metal solidifies faster than the bubble rises up to the surface. As a result, the gas bubble remains inside the cooling metal resulting in a process of residual porosity.

Such porosity is also observed experimentally as Fig. 4 presents. The presented numerical model then captures this phenomenon. This particularity will be used in further investigations for laser welding stability and process efficiency. Porosity formation dynamics and its final size are very sensitive to the value of the surface tension, which should also be known more precisely in the same way as the absorptivity.

Power modulation has already been presented as an effective method to enhance weld quality and suppress porosity occurrence.[18,33] This welding strategy could be investigated numerically in a further study with the present model.

V. CONCLUSION AND OUTLOOKS

A numerical model of spot laser welding has been developed including a self-consistent ray-tracing algorithm able to capture irradiance variations with keyhole geometry fluctuations. The latter is compared with experimental cross sections and gives satisfactory results. The model also captures melt pool behavior found in the literature.

A strong effect of material absorptivity on penetration dynamic is presented highlighting the need for more accurate properties knowledge for a numerical purpose.

The model is globally validated for intermediate keyhole aspect ratios (2–4). Further investigations will be made to improve the model and compare it with up-to-date x-ray measurements.

An extension to a complete 3D description will be made in the next development steps to investigate the effect of high power combined with high welding speed on the stability and efficiency of the laser welding process.

ACKNOWLEDGMENTS

The authors are grateful to Rudolf Weber, Michael Sawannia, Frauke Faure, and Christian Hagenlocher from IFSW Stuttgart for

their helpful discussions as part of the FASTLAS project supported by Agence Nationale de la Recherche (ANR) and Deutsche Forschungsgemeinschaft (DFG).

AUTHOR DECLARATIONS

Conflict of Interests

The authors have no conflicts to disclose.

Author Contributions

Julien Daligault: Conceptualization (equal); Formal analysis (equal); Investigation (equal); Methodology (equal); Software (equal); Validation (equal); Visualization (equal); Writing – original draft (equal); Writing – review & editing (equal). **Morgan Dal:** Conceptualization (equal); Funding acquisition (lead); Methodology (equal); Project administration (lead); Resources (lead); Software (equal); Supervision (lead); Writing – original draft (equal); Writing – review & editing (equal). **Cyril Gorny:** Investigation (equal); Validation (equal); Writing – original draft (equal); Writing – review & editing (equal). **Frédéric Coste:** Investigation (equal); Validation (equal); Writing – original draft (equal); Writing – review & editing (equal). **Rémy Fabbro:** Conceptualization (supporting); Supervision (supporting); Writing – original draft (equal); Writing – review & editing (equal).

REFERENCES

[1]A. R. Sufizadeh and S. A. A. Akbari Mousavi, "Investigation of Nd:YAG pulsed laser dissimilar welding of AISI 4340 and AISI 316L stainless steels on weld geometry and mechanical properties," Mech. Ind. **18**, 512–523 (2017).
[2]S. Katayama, "Laser welding of aluminium alloys and dissimilar metals," Weld. Int. **18**, 618–625 (2004).
[3]R. Fabbro, "Depth dependence and keyhole stability at threshold, for different laser welding regimes," Appl. Sci. **10**, 1487–1509 (2020).
[4]Y. A. Mayi, M. Dal, P. Peyre, M. Bellet, C. Metton, C. Moriconi, and R. Fabbro, "Transient dynamics and stability of keyhole at threshold investigated by finite element modeling," J. Laser Appl. **33**, 012024 (2021).
[5]M. Courtois, M. Carin, P. L. Masson, S. Gaied, and M. Balabane, "A new approach to compute multi-reflections of laser beam in a keyhole for heat transfer and fluid flow modelling in laser welding," J. Phys. Appl. Phys. **46**, 505305 (2013).
[6]M. Medale, C. Touvrey, and R. Fabbro, "An axi-symmetric thermo-hydraulic model to better understand spot laser welding," Eur. J. Comput. Mech. **17**, 795–806 (2008).
[7]J. Trapp, "In situ absorptivity measurements of metallic powders during laser powder-bed fusion additive manufacturing," Appl. Mater. Today **9**, 341–349 (2017).
[8]R. Cunningham, C. Zhao, N. Parab, C. Kantzos, J. Pauza, K. Fezzaa, T. Sun, and A. D. Rollett, "Keyhole threshold and morphology in laser melting revealed by ultrahigh-speed x-ray imaging," Science **363**, 849–852 (2019).
[9]G. Nordet, C. Gorny, Y. Mayi, J. Daligault, M. Dal, A. Effernelli, E. Blanchet, F. Coste, and P. Peyre, "Absorptivity measurements during laser powder bed fusion of pure copper with a 1 kW CW green laser," Opt. Laser Technol. **147**, 107612 (2022).
[10]A. Rubenchik, S. Wu, S. Mitchell, I. Golosker, M. LeBlanc, and N. Peterson, "Direct measurements of temperature-dependent laser absorptivity of metal powders," Appl. Opt. **54**, 7230–7233 (2015).
[11]R. Fabbro, "Melt pool and keyhole behaviour analysis for deep penetration laser welding," J. Phys. D: Appl. Phys. **43**, 445501 (2010).
[12]M. Mattern, T. Weigel, and A. Ostendorf, "Temporal temperature evolution in laser micro-spot welding of copper considering temperature-dependent material parameters," Mater. Res. Express **5**, 066545 (2018).
[13]A. Heider, "High-speed X-ray analysis of spatter formation in laser welding of copper," Phys. Proc. **41**, 112–118 (2013).
[14]A. Heider, P. Stritt, R. Weber, and T. Graf, "High-power laser sources enable high-quality laser welding of copper," in *International Congress on Applications of Lasers & Electro-Optics*, *San Diego, CA, October 2014* (Laser Institute of America, Orlando, FL, 2014), pp. 343–348.
[15]S. Engler, R. Ramsayer, and R. Poprawe, "Process studies on laser welding of copper with brilliant green and infrared lasers," Phys. Proc. **12**, 339–346 (2011).
[16]L. Alter, A. Heider, and J.-P. Bergmann, "Investigations on copper welding using a frequency-doubled disk laser and high welding speeds," Proc. CIRP **74**, 12–16 (2018).
[17]A. Hess, A. Heider, R. Schuster, R. Weber, and T. Graf, "Benefits from combining laser beams with different wavelengths (green and IR) for copper welding," in *International Congress on Applications of Lasers & Electro-Optics*, *Anaheim, CA, September 2010* (Laser Institute of America, Orlando, FL, 2010), pp. 540–546.
[18]A. Heider, R. Weber, D. Herrmann, P. Herzog, and T. Graf, "Power modulation to stabilize laser welding of copper," J. Laser Appl. **27**, 022003 (2015).
[19]F. Faure, R. Weber, and T. Graf, "Influence of beam parameters on the capillary formation and the depth progress in laser spot welding of copper," in *Lasers in Manufacturing Conference*, online, June 2021 (German Scientific Laser Society, Hannover, Germany, 2021).
[20]F. Fetzer, C. Hagenlocher, R. Weber, and T. Graf, "Geometry and stability of the capillary during deep-penetration laser welding of AlMgSi at high feed rates," Opt. Laser Technol. **133**, 106562 (2021).
[21]V. Bruyere, C. Touvrey, and P. Namy, "A phase field approach to model laser power control in spot laser welding," COMSOL Conference, Cambridge (2014), p. 6.
[22]H. Ki, J. Mazumder, and P. S. Mohanty, "Modeling of laser keyhole welding: Part I. Mathematical modeling, numerical methodology, role of recoil pressure, multiple reflections, and free surface evolution," Metall. Mater. Trans. A **33**, 1817–1830 (2002).
[23]B. Liu, G. Fang, L. Lei, and W. Liu, "A new ray tracing heat source model for mesoscale CFD simulation of selective laser melting (SLM)," Appl. Math. Model. **79**, 506–520 (2020).
[24]B. Liu, G. Fang, L. Lei, and W. Liu, "Experimental and numerical exploration of defocusing in laser powder Bed fusion (LPBF) as an effective processing parameter," Opt. Laser Technol. **149**, 107846 (2022).
[25]P. P. Crooker, W. B. Colson, and J. Blau, "Representation of a Gaussian beam by rays," Am. J. Phys. **74**, 722–727 (2006).
[26]P. Yue, J. J. Feng, C. Liu, and J. Shen, "A diffuse-interface method for simulating two-phase flows of complex fluids," J. Fluid Mech. **515**, 293–317 (2004).
[27]K. C. Mills, *Recommended Values of Thermophysical Properties for Selected Commercial Alloys* (Woodhead, Cambridge, 2002).
[28]D. R. Lide, G. Baysinger, S. Chemistry, L. I. Berger, R. N. Goldberg, and H. V. Kehiaian, *CRC Handbook of Chemistry and Physics* (National Institutes of Standards and Technology, New York, 2003), p. 2661.
[29]A. Gouffé, "Corrections d'ouverture des corps noirs artificiels compte tenu des diffusions multiples internes," Rev. Opt. **24**, 1–10 (1945).
[30]J. Ye, S. A. Khairallah, A. M. Rubenchik, M. F. Crumb, G. Guss, J. Belak, and M. J. Matthews, "Energy coupling mechanisms and scaling behavior associated with laser powder Bed fusion additive manufacturing," Adv. Eng. Mater. **21**, 1900185 (2019).
[31]P. Johnson and R. Christy, "Optical constants of transition metals: Ti, V, Cr, Mn, Fe, Co, Ni, and Pd," Phys. Rev. B **9**, 5056–5070 (1974).
[32]D. Bergström, J. Powell, and A. F. H. Kaplan, "The absorption of laser light by rough metal surfaces–A three-dimensional ray-tracing analysis," J. Appl. Phys. **103**, 103515 (2008).
[33]A. Matsunawa, J.-D. Kim, and S. Katayama, "Porosity formation in laser welding—Mechanisms and suppression methods," in *International Congress on Applications of Lasers & Electro-Optics*, *San Diego, CA, November 1997* (Laser Institute of America, Orlando, FL, 1997), pp. G73–G82.